Geoscience Frontiers 11 (2020) 1323–1335

HOSTED BY

Contents lists available at ScienceDirect

Geoscience Frontiers

journal homepage: www.elsevier.com/locate/gsf

Research Paper

Integrated U–Pb, Lu–Hf and (U–Th)/He analysis of zircon from the Banxi Sb deposit and its implications for the low-temperature mineralization in South China

Huan Li [a,*], Martin Danišík [b], Zhe-Kai Zhou [c], Wei-Cheng Jiang [d], Jing-Hua Wu [a,d]

[a] Key Laboratory of Metallogenic Prediction of Nonferrous Metals and Geological Environment Monitoring, Ministry of Education, School of Geosciences and Info-Physics, Central South University, Changsha 410083, China
[b] John de Laeter Centre, TIGeR, Curtin University, Bentley, 6845, Australia
[c] Department of Earth Resources Engineering, Faculty of Engineering, Kyushu University, Fukuoka, 819-0395, Japan
[d] Department of Resources Science and Engineering, Faculty of Earth Resources, State Key Laboratory of Geological Processes and Mineral Resources, China University of Geosciences, Wuhan 430074, China

ARTICLE INFO

Handling Editor: Vinod Oommen Samuel

Keywords:
Sb (Au–Hg) deposits
U–Pb - Lu–Hf - (U–Th)/He triple-dating
Basement rocks
Fluid circulation
Zircon

ABSTRACT

Low-temperature Sb (Au–Hg) deposits in South China account for more than 50% of the world's Sb reserves, however, their genesis remains controversial. Here we report the first study that integrates U–Pb and Lu–Hf analysis by LA-(MC)-ICPMS and conventional (U–Th)/He analysis, all applied to single zircon crystals, in an attempt to constrain the origin and timing of world-class Sb (Au–Hg) deposits in Banxi (South China). Zircon separated from a quartz-stibnite ore and an altered country rock samples revealed similar U–Pb age spectra defining two major populations – Paleoproterozoic (~1900–2500 Ma) and Neoproterozoic (~770 Ma), which are characterized by variable $\varepsilon_{Hf}(t)$ values (–10.7 to 9.1 and –16.5 to 11.2, respectively) and Hf crustal model ages (T_{DM}^{C}) (2.48 to 3.24 Ga and 0.97 to 2.71 Ga, respectively). The U–Pb age and Hf isotopic features of the zircons are consistent with the Banxi Group in the region, indicating that the zircons involved in the low-temperature hydrothermal system were originally from the Banxi Group country rocks. Thirty-three mineralization-related zircon crystals yielded a mean (U–Th)/He age of 123.8 ± 3.8 Ma, which is interpreted to represent the timing of the latest low-temperature mineralization stage of the Banxi Sb deposit. The combined U–Pb, Lu–Hf and (U–Th)/He data suggest that Precambrian basement rocks were the major contributors to the low-temperature mineralization, and that Early Cretaceous (130–120 Ma) could be the most important ore-forming epoch for the Sb deposits in South China. This study also demonstrates the analytical feasibility of integrated U–Pb - Lu–Hf - (U–Th)/He "triple-dating", all applied to single zircon crystals. This approach reveals the full evolution of zircon, from its origin of the magmatic source, through its crystallization and low-temperature cooling. Although this study demonstrates the usefulness of this integrated approach in dating low-temperature mineralization, it has great potential for zircon provenance and other studies that may benefit from the large amount of information that can be extracted from single zircon crystals.

1. Introduction

The isotopic signatures in zircon, a common accessory mineral, have been studied in a wide range of mineral systems with implications for exploration. For example, the low-temperature (U–Th)/He system, which is sensitive to geological processes over the 160–200 °C range (e.g., Reiners, 2005), has been successfully applied to dating epithermal mineralization (Cunningham et al., 1996; McInnes et al., 2005; Harris et al., 2008; Betsi et al., 2012; Liu et al., 2014; Fu et al., 2019a, b). The high-temperature Lu–Hf and U–Pb systems, on the other hand, can contribute to petrogenetic interpretation by unraveling the magmatic source and the origin of zircons, respectively (Li et al., 2012; Zeng et al., 2013; Li et al., 2018a, b; Wu et al., 2018). Recent advances in technological and methodological capabilities (e.g., micro-sampling by lasers;

* Corresponding author.
E-mail address: lihuan@csu.edu.cn (H. Li).
Peer-review under responsibility of China University of Geosciences (Beijing).

https://doi.org/10.1016/j.gsf.2020.01.004
Received 15 May 2019; Received in revised form 10 October 2019; Accepted 1 January 2020
Available online 20 January 2020
1674-9871/© 2020 China University of Geosciences (Beijing) and Peking University. Production and hosting by Elsevier B.V. This is an open access article under the CC BY-NC-ND license (http://creativecommons.org/licenses/by-nc-nd/4.0/).

improved sensitivity of mass-spectrometers) now allow several analytical techniques to be applied to the same crystal, addressing different aspects of ore genesis and opening up new avenues for studying minerals systems. However, reliability of the integrated multi-isotopic analysis on single zircon grains and its practicality for studying ore deposits yet need to be explored.

Low-temperature deposits are widely developed in South China. These deposits are mainly situated at the southern margin of Yangtze Block along the Jiangnan Orogen, forming the largest Sb (Au–Hg) belt in the world (Fig. 1). This belt accounts for more than 50% of the Sb reserves of the world, and ~10% of the Au reserves and 80% of the Hg reserves of China (Hu et al., 2017). This NEE-striking ore belt stretches from Anhui in the east, crosses into Hubei, Jiangxi, Hunan, Guizhou and Guangxi, and reaches at Yunnan in the west, with a length of ~1900 km and width of ~200 km (Hu et al., 2007). World-class Sb (Au–Hg) deposits such as Xikuangshan, Banxi, Woxi, Zhazixi, Dachang, Dushan, Muli, Qinglong and Maxiong are the most typical representatives in this belt, with ore-forming temperatures of 100–250 °C (mostly 160–200 °C) (Hu et al., 2016). Although abundant research has been carried out on these deposits (e.g., Yang et al., 2006a, b; Gu et al., 2007; Liang et al., 2014; Hu et al., 2017; Hu and Peng, 2018; Li et al., 2018c), the timing of mineralization is highly controversial (Peng et al., 2003a, b; Wang et al., 2012a; Fu et al., 2016), and the source of ore-forming materials is still under debate (Fan et al., 2004; Peng and Frei, 2004; Wang et al., 2012b; Xu et al., 2017; Xie et al., 2018).

In this study we seek to explore a novel analytical concept that applies three different isotopic systems to single zircon crystals. We target zircons from the Banxi Sb deposit and analyze these by laser ablation inductively coupled plasma mass spectrometry (LA-ICPMS) for U–Pb, laser ablation multi-collector inductively coupled plasma mass spectrometry (LA-(MC)-ICPMS) for Lu–Hf and by conventional (U–Th)/He dating method. This approach enables us to reconstruct the complete history of zircon and provide new insights into the genesis low-temperature mineralization in South China. The aim of this study is to test and demonstrate the feasibility of the integrated U–Pb - Lu–Hf - (U–Th)/He "triple-dating" of single zircon grains to effectively exploit all the geochronological and geochemical information from zircon, and apply this approach as a novel tool to study ore deposits.

2. Geology

The South China Block was amalgamated from the Yangtze Block to the northwest and the Cathaysia Block to the southeast during Neoproterozoic (Zhao, 2015). As the boundary between the two blocks, the Jiangnan Orogen is assumed to record continent–arc–continent collision between the Yangtze and Cathaysia blocks (Fig. 1; Cui et al., 2017; Su et al., 2017; Li et al., 2019a). This orogen mainly comprises Neoproterozoic weakly metamorphosed volcanic-sedimentary basement rocks (e.g., Banxi Group) and unmetamorphosed Sinian cover, with intrusions of middle Neoproterozoic peraluminous S-type granites (Zhao and Cawood, 2012; Song et al., 2017).

The Sb deposits in South China are mainly distributed in and around the Jiangnan Orogen, with no or little spatial association to magmatic activity (Fig. 1). These deposits can be classified into three types based on ore-forming elements and host rocks: Sb–Au–W type (e.g., Woxi), Sb-only type (e.g., Xikuangshan) and Sb–F type (e.g., Qinglong) (Hu et al., 2007). The Sb–Au–W deposits are mainly hosted by Neoproterozoic epimetamorphic clastic rocks in the Jiangnan Orogen, with stibnite, scheelite and native gold as the ore minerals and quartz as the major gangue mineral (Liang et al., 2014; Li et al., 2019b). The Sb-only deposits are mainly hosted in Devonian sedimentary formations in central Hunan, with quartz–stibnite and calcite–stibnite ore assemblages (Yang et al., 2006a, b). The Sb–F deposits dominantly develop in the Lower Permian limestone-pyroclastic rocks in southwest Guizhou, with stibnite, pyrite, quartz, fluorite and calcite as the major minerals in ores (Chen et al., 2016).

Located at the southeast margin of the Jiangnan Orogen, the Banxi Sb deposit can be regarded as a transition type between Sb–Au–W type and Sb-only type. It has been mined for 100 years, and recent exploration indicates a total Sb metal reserve of up to 100,000 tons. Quartz–stibnite veins are hosted in the Banxi Group epimetamorphic clastic rocks which can be lithologically divided into three members including tuff, tuffaceous siltstone, tuffaceous slate, sericite slate, sandy slate and silty slate (Fig. 2a). Ore veins are controlled by a series of NE-striking faults, forming several subparallel ore belts. Among them, the actively mined No. 2 ore belt in the Jiangjiachong anticline region is the largest and most representative. It is characterized by an elongated "S" shape in plan view, with a full-length of over 2000 m. Ore veins in this belt are NW-inclined with a varied dip direction of 315°–350° and a dip angle of 46°–89° (Fig. 2b), with thickness of 0.3–1 m and a Sb grade of 0.02%–64.5%. Three hydrothermal stages can be differentiated within the Banxi deposit: quartz stage (Fig. 3a), quartz-stibnite stage (Fig. 3b), and stibnite stage (Fig. 3c). Among them, the quartz–stibnite and stibnite stages are the most developed. Wall-rock alterations include strong

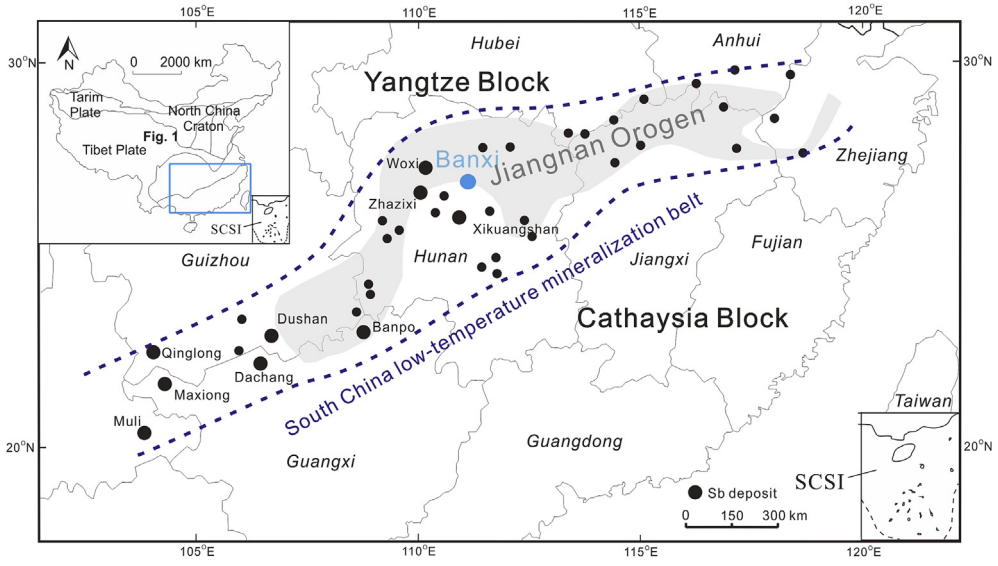

Fig. 1. Simplified tectonic map of the South China Block, showing the distribution of major Sb (Au–Hg) deposits in the South China low-temperature mineralization belt (after Ma, 1999; Wang et al., 2014). SCSI, South China Sea Islands.

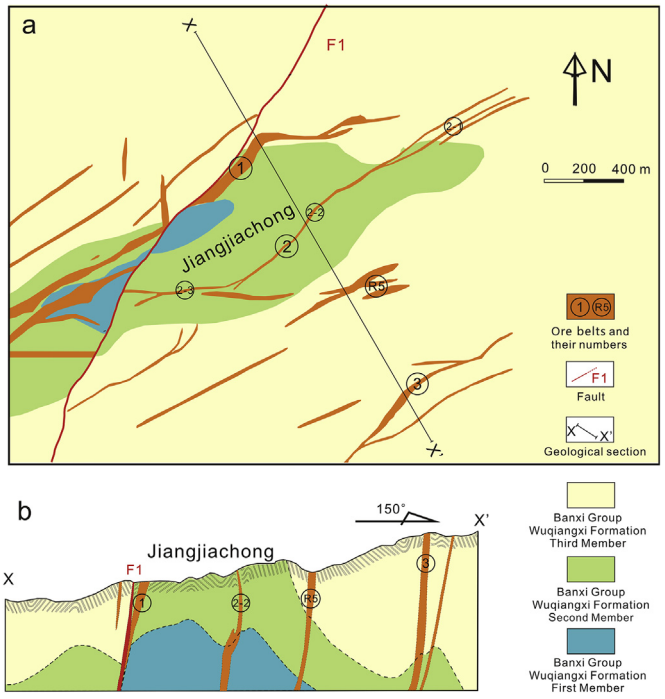

Fig. 2. (a) Geological map and (b) cross section of the Banxi Sb deposit.

arsenopyritization (Fig. 3d) and silicification (Fig. 3e) developed close to ore bodies, and weak pyritization, calcilization and chloritization (Fig. 3f) further away from mineralization. In addition, decolourization is widely developed in the Banxi Group tuffaceous rocks, such as in the tuffaceous slate (Fig. 3g), tuffaceous siltstone (Fig. 3h) and the tuff (Fig. 3i).

3. Samples and methods

Typical quartz-stibnite ore and hydrothermally altered country rock samples were taken from underground exploration tunnels at different levels of the Banxi deposit. One quartz–stibnite ore and one altered country rock were chosen for zircon analysis in this study. The quartz–stibnite ore was sampled from the No. 2-3 ore vein at Level 15 (–415 m, ~600 m from the surface). It has a massive structure (Fig. 4a), with fine-grained, subhedral-anhedral stibnite intergrown with quartz (Fig. 4b). The altered tuffaceous siltstone was collected close to the No. 2-2 ore vein at Level 6 (–30 m, ~200 m from the surface). It has a massive banded structure with obvious silicification, pyritization and arsenopyritization (Fig. 4c), with quartz and feldspar as the major original minerals and hydrothermal pyrite and arsenopyrite is also present (Fig. 4d).

Zircon separation was carried out using standard techniques, with individual crystals hand-picked using a binocular microscope, mounted in epoxy resin, and polished to expose the grain center. Cathodoluminescence (CL) images were taken at Beijing GeoAnalysis Co., Ltd. Zircon U–Pb isotopic analyses were analyzed *in situ* using LA-ICPMS at the State Key Laboratory of Geological Processes and Mineral Resources (GPMR), China University of Geosciences (Wuhan). Laser sampling was performed using an excimer laser ablation system consisting of a GeoLas 2005 with an Agilent 7500a ICPMS used to acquire ion-signal intensities. The beam diameter was 32 μm for all zircons. Each analysis incorporated a background acquisition interval of ~20–30 s (gas blank) followed by a 40 s data acquisition interval. Zircon 91500 (Wiedenbeck et al., 2004) was used as the reference standard for U–Pb dating, and was analyzed twice for every five unknowns. Time-dependent drift was corrected using a linear interpolation (with time) for every five analyses according to variations of 91500. Zircon GJ-1 was analyzed as secondary standard and yielded a weighted mean $^{206}Pb/^{238}U$ age of 598.9 ± 3.32 Ma (2σ, $n = 8$), consistent with the recommended values within uncertainty (599.81 ± 1.7 Ma (2σ); Jackson et al., 2004). Detailed analytical conditions and procedures for zircon U–Pb LA-ICPMS dating are described in Liu et al. (2010). Off-line selection and integration of background and analytical signals, time-drift correction, and quantitative calibration for zircon U–Pb dating were performed using ICPMSDataCal 8.3. Common Pb was

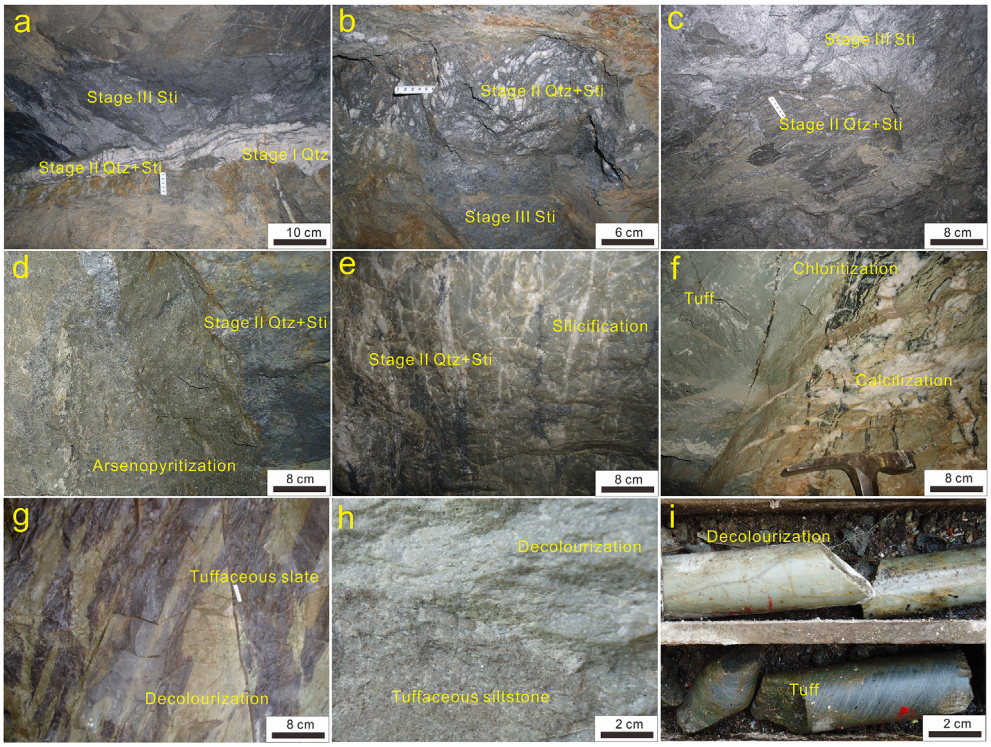

Fig. 3. Field occurrences of ore bodies and alteration zones at the Banxi Sb deposit. (a) Stage I quartz, stage II quartz-stibnite and stage III stibnite veins developed sequentially in the Banxi Group clastic rocks; (b) stage II quartz-stibnite ores show shear deformation characteristics, in contrast to the undeformed stage III stibnite; (c) stage III stibnite superimposed on the stage II quartz-stibnite; (d) strong arsenopyritization developed close to Sb ore bodies; (e) intense silicification occur near Sb ore bodies; (f) weak calcilization and chloritization appear far away from Sb mineralization; (g) decolourization in the tuffaceous slate; (h) decolourization in the tuffaceous siltstone; (i) decolourization in the tuff. Qtz: quartz; Sti: stibnite.

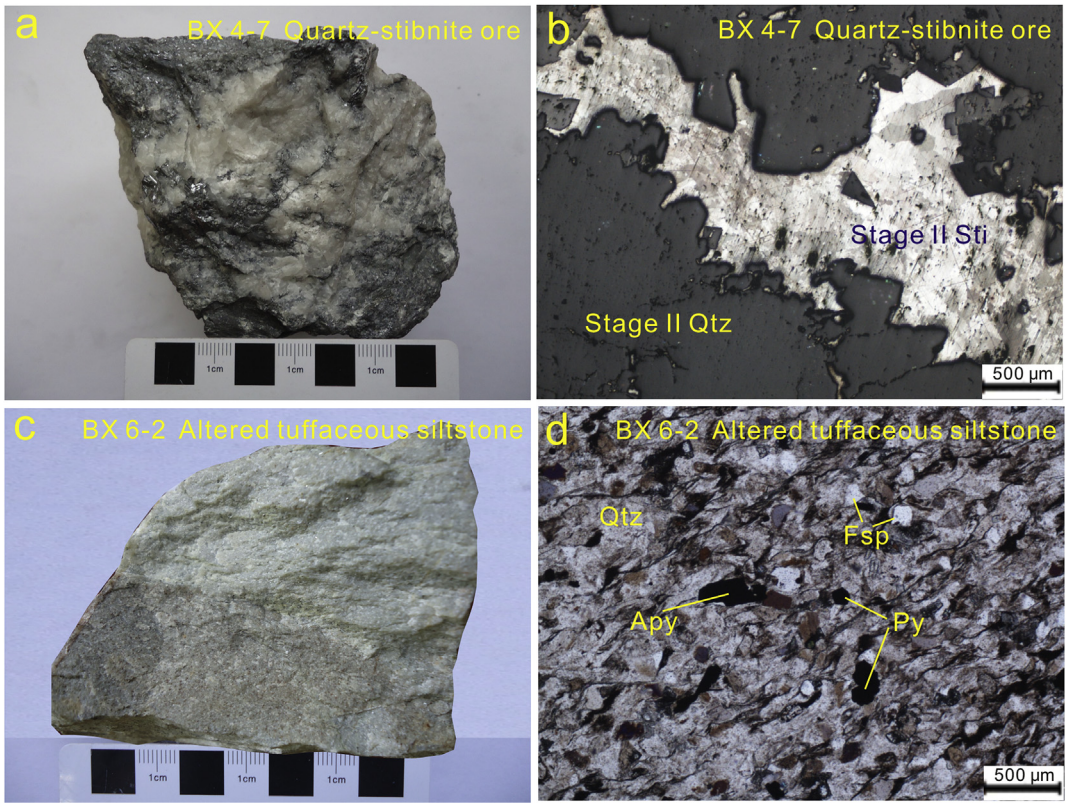

Fig. 4. (a) Hand specimen image of sample BX4-7, showing intergrowth of quartz and stibnite with a massive structure; (b) micrograph of sample BX4-7, fine-grained, subhedral–anhedral stibnite intergrown with quartz; (c) hand specimen image of sample BX6-2, showing massive banded structure with obvious silicification, pyritization and arsenopyritization; (d) macrograph of sample BX6-2, quartz and feldspar appear as major original minerals and pyrite and arsenopyrite occur as hydrothermal minerals. Qtz: quartz; Sti: stibnite; Apy: arsenopyrite; Py: pyrite.

corrected based on the method proposed by Anderson (2002) with concordia diagrams and weighted mean calculations made using Isoplot 4.5 (Ludwig, 2003).

In situ analysis of zircon Lu–Hf isotopes was carried out by LA-MC-ICPMS at GPMR, with a spot size of 44 μm. The ablation spots for Hf isotope analyses were located over the U–Pb age analysis positions on each grain. Interference of ^{176}Lu on ^{176}Hf was corrected by measuring the intensity of interference-free ^{175}Lu, with a ^{176}Lu/^{175}Lu ratio of 0.02669 (De Biévre and Taylor, 1993) used to calculate ^{176}Lu/^{177}Hf. The isobaric interference of ^{176}Yb on ^{176}Hf was corrected using a ^{176}Yb/^{172}Yb ratio of 0.5886 (Chu et al., 2002). Detailed operating conditions and analytical methods for LA-MC-ICPMS are described in Hu et al. (2012). Three different zircon standards (91500, TEM and GJ-1) were measured to correct and monitor Hf isotopic values. As the primary reference material, 91500 was analyzed twice every 8 unknowns and both GJ-1 and TEM standard zircons were analyzed twice at the beginning and ending of the run. The ^{176}Hf/^{177}Hf results obtained for 91500 are within error (0.282304 ± 0.000012 (95% conf., n = 10) of the recommended Hf isotopic values (0.282306 ± 0.00004) (Wiedenbeck et al., 2004). The secondary standards GJ-1 and TEM, treated as unknowns, yielded ^{176}Hf/^{177}Hf ratios of 0.282010 ± 0.000020 (95% conf., n = 4) and 0.282688 ± 0.000019 (95% conf., n = 4), respectively, which agree with the recommended values within uncertainty (0.282000 ± 5 for GJ-1, Morel et al., 2008; and 0.282677 for TEM, Hu et al., 2012). Off-line selection and integration of analyte signals, and mass bias calibrations were performed using ICPMSDataCal (Liu et al., 2010). A decay constant of 1.867 × 10^{-11} y^{-1} was adopted for ^{176}Lu (Soderlund et al., 2004). The initial ^{176}Hf/^{177}Hf ratio, denoted as $\varepsilon_{Hf}(t)$, was calculated relative to the chondritic reservoir with a ^{176}Hf/^{177}Hf ratio of 0.282785 and ^{176}Lu/^{177}Hf of 0.0336 (Bouvier et al., 2008). Single stage Hf model ages (T_{DM1}) were calculated relative to the depleted mantle with a present day ^{176}Hf/^{177}Hf ratio of 0.28325 and ^{176}Lu/^{177}Hf of 0.0384 (Vervoort and Blichert-Toft, 1999), and crust Hf model ages (T_{DM}^{C}) were calculated by assuming a mean ^{176}Lu/^{177}Hf value of 0.015 for average continental crust (Griffin et al., 2002).

(U–Th)/He dating of zircon was carried out at the Low Temperature Thermochronology facility in the John de Laeter Centre in Perth, Australia. One of the critical requirements for successful multi-dating approaches is that all radiometric decay schemes used leave the other isotopic systems undisturbed during the multiple analytical steps. It has been shown that the localized laser-induced heating of the excimer laser beam in LA-(MC)-ICPMS analysis can affect the accuracy of the U–Pb system in zircon, which is unaffected at temperatures of <900 °C (Lee et al., 1997; Marillo-Sialer et al., 2014). Given that He diffuses out of zircon at much lower temperatures (~180 °C at geological time-scale; Reiners, 2005), local heating during ablation could impact the (U–Th)/He systematics in zircon crystals that have been analyzed for U–Pb and Lu–Hf prior to conventional (U–Th)/He dating. To test the potential impact of laser ablation on (U–Th)/He systematics, an experiment was conducted in which two types of zircon from each sample were analyzed: The first type consisted of six pristine zircon crystals that were handpicked from the mineral concentrates; the second type consisted of zircon crystals that were analyzed by LA-(MC)-ICPMS for U–Pb and Lu–Hf. These zircon grains were plucked out of the epoxy mounts.

Both types of zircon were analyzed by conventional (U–Th)/He dating procedures outlined in Danišík et al. (2012). Single zircon crystals were photographed under a microscope and measured (in 3D) in order to calculate the alpha ejection correction (Farley et al., 1996). Crystals were then loaded in Nb microtubes, degassed at ~1250 °C under ultra-high vacuum using a focused ~980-nm diode laser beam and analyzed for ^{4}He on a noble-gas mass-spectrometer (Pfeiffer Prisma™) by isotope dilution using a ^{3}He spike. Each gas extraction was followed by a re-extract (Farley, 2002) to ensure complete degassing of the zircon grains. Following He measurements, zircon-Nb packages were retrieved

from the He extraction system, spiked with ^{235}U and ^{230}Th, and dissolved in pressure digestion vessels (Parr bombs) using HF–HNO_3 and HCl acids (Evans et al., 2005). Diluted solutions were analyzed by isotope dilution for ^{232}Th and ^{238}U and by external calibration for ^{147}Sm on an Agilent 7500 ICP-MS. Measured U, Th, Sm and He abundances were used to calculate raw (U–Th)/He ages. The raw (U–Th)/He ages were corrected for alpha-ejection after Farley et al. (1996) thereby assuming homogeneous distribution of parent nuclides and applying a correction for the mineral portion removed by polishing to the zircon previously analyzed by LA-(MC)-ICPMS. The total analytical uncertainty (TAU) was calculated as the square root of the sum of the squares of weighted uncertainties on the U, Th, Sm and He abundances and was used to calculate the error on the raw (U–Th)/He ages.

4. Results

4.1. Zircon morphology and U–Pb geochronology

Zircons separated from the quartz-stibnite ore (sample BX4-7) and the altered tuffaceous siltstone (sample BX6-2) show similar characteristics in CL images (Fig. 5). They have euhedral prismatic shapes, and some with weak psephicity. Most range from 40 to 80 μm in diameter, with length/width ratios of 1:1 to 2:1, showing clear oscillatory zonation, indicating a magmatic origin. In addition, a few of the crystals show dark and weak zonation on CL images.

The zircon U–Pb dating results for 50 zircons are shown in Table 1. The age variations ($^{206}Pb/^{238}U$ age for zircons younger than 1000 Ma and $^{206}Pb/^{207}Pb$ age for those older than 1000 Ma) are similar within two samples, ranging from 773 to 2531 Ma for sample BX4-7 and from 696 to 2544 Ma for sample BX6-2, respectively. They can be assigned to two major groups: Neoproterozoic (~770 Ma) ($n = 31$) and Paleoproterozoic (~1900–2500 Ma) ($n = 16$) (Fig. 6). For CL images, the Neoproterozoic zircons are bright and show oscillatory zoning, whereas the Paleoproterozoic zircons are dark and weakly zoned (Fig. 5). Seven Neoproterozoic zircons yielded a concordant U–Pb age of 776 ± 11 Ma (MSWD = 0.01) for sample BX4-7 (Fig. 6a), and the other twenty-two Neoproterozoic zircons yielded a concordant U–Pb age of 770 ± 4 Ma (MSWD = 0.07) for sample BX6-2 (Fig. 6b).

4.2. Zircon Hf isotopes

Zircon Hf isotopic results and related parameters for the ore and country rock are given in Table 2. On the whole, the Hf isotopic ratios vary significantly within each sample, and no obvious differences in value ranges are observed among the two samples (Fig. 7a, b). For the Neoproterozoic zircons (~770 Ma), the $^{176}Yb/^{177}Hf$, $^{176}Lu/^{177}Hf$ and $^{176}Hf/^{177}Hf$ values range from 0.014420 to 0.099458, from 0.000505 to 0.003370 and from 0.281836 to 0.282628, respectively, with initial $^{176}Hf/^{177}Hf$ values ranging from 0.281824 to 0.282605. The $\varepsilon_{Hf}(t)$ values of the Neoproterozoic zircons range from –16.5 to 11.2 (Fig. 7a), with corresponding Hf model ages (T_{DM}) and crustal model ages (T_{DM}^{C}) ranging from 0.90 to 1.98 Ga and from 0.97 to 2.71 Ga (Fig. 7b), respectively. For the Paleoproterozoic zircons (~1900–2500 Ma), the $^{176}Yb/^{177}Hf$, $^{176}Lu/^{177}Hf$, and $^{176}Hf/^{177}Hf$ values are much lower and range from 0.009742 to 0.025773, from 0.000301 to 0.000877, and from 0.281247 to 0.281401, respectively, with initial $^{176}Hf/^{177}Hf$ values ranging from 0.281236 to 0.281412. The $\varepsilon_{Hf}(t)$ values of the Paleoproterozoic zircons range from –10.7 to 9.1 (Fig. 7a), with relatively older corresponding Hf model ages (T_{DM}) and crustal model ages (T_{DM}^{C}) ranging from 2.50 to 2.74 Ga and from 2.48 to 3.24 Ga (Fig. 7b), respectively.

4.3. Zircon (U–Th)/He thermochronology

The zircon (U–Th)/He dating results for thirty-three zircons are shown in Table 3. The (U–Th)/He ages from all zircon crystals are in the range of 101.5–139.9 Ma, and form one uniform population with no significant differences between the replicates. There is no difference between the (U–Th)/He ages obtained on pristine and previously ablated zircon crystals, suggesting that the laser-induced heating during ablation had a negligible impact on (U–Th)/He systematics. Thirteen zircon grains

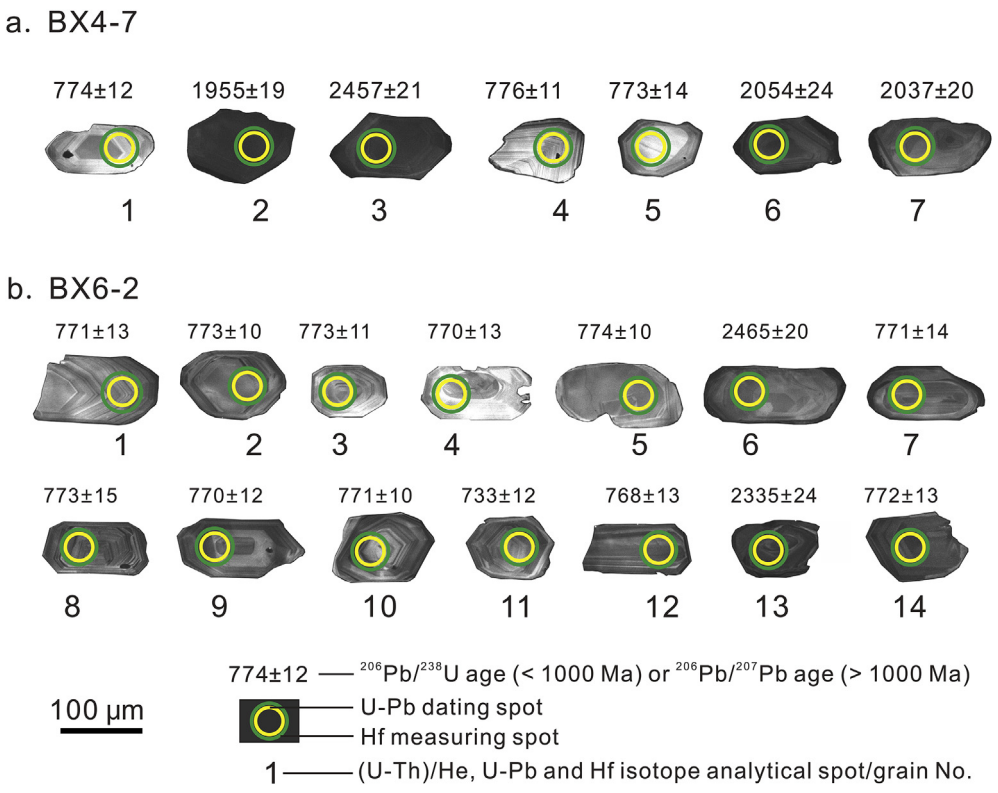

Fig. 5. CL-images of (U–Th)/He-analyzed zircons from samples (a) BX4-7 and (b) BX6-2, showing U–Pb dating and Hf measuring spots.

Table 1
Zircon LA-ICPMS U–Pb isotopic compositions of the Banxi Sb deposit.

Spot No.	Isotopic ratios						Apparent age (Ma)					
	$^{207}Pb/^{206}Pb$	1σ	$^{207}Pb/^{235}U$	1σ	$^{206}Pb/^{238}U$	1σ	$^{207}Pb/^{206}Pb$	1σ	$^{207}Pb/^{235}U$	1σ	$^{206}Pb/^{238}U$	1σ
Sample BX4-7, quartz-stibnite ore												
BX4-7-01	0.073146	0.004819	1.305649	0.071147	0.127566	0.002091	1018	133	848	31	774	12
BX4-7-02	0.119902	0.002229	6.012919	0.115018	0.362118	0.003798	1955	19	1978	17	1992	18
BX4-7-03	0.160015	0.003290	10.157195	0.207820	0.458336	0.004597	2457	21	2449	19	2432	20
BX4-7-04	0.062831	0.003029	1.100943	0.052832	0.127926	0.001934	702	301	754	26	776	11
BX4-7-05	0.069845	0.004503	1.243762	0.075423	0.127400	0.002516	924	132	821	34	773	14
BX4-7-06	0.126652	0.003231	6.518884	0.166952	0.372473	0.004828	2054	24	2048	23	2041	23
BX4-7-07	0.125544	0.002984	6.379027	0.159372	0.367064	0.004523	2037	20	2029	22	2016	21
BX4-7-08	0.083296	0.004276	1.466868	0.080838	0.127509	0.002449	1276	100	917	33	774	14
BX4-7-09	0.060202	0.003121	1.051049	0.052011	0.128017	0.001994	609	113	729	26	777	11
BX4-7-10	0.119473	0.002548	5.311766	0.126243	0.321697	0.004826	1950	39	1871	20	1798	24
BX4-7-11	0.116218	0.002411	3.673075	0.110242	0.227493	0.005038	1899	37	1566	24	1321	26
BX4-7-12	0.077663	0.003552	1.561752	0.068542	0.146802	0.002286	1139	86	955	27	883	13
BX4-7-13	0.115026	0.002533	2.186299	0.050486	0.136987	0.001279	1881	40	1177	16	828	14
BX4-7-14	0.155819	0.003057	9.847045	0.208382	0.455677	0.004963	2411	33	2421	20	2420	22
BX4-7-15	0.067187	0.004831	1.186588	0.088107	0.127826	0.002281	843	150	794	41	775	13
BX4-7-16	0.071949	0.005101	1.247898	0.078957	0.128202	0.002800	984	146	822	36	778	16
BX4-7-17	0.235427	0.004109	18.997626	0.378389	0.581499	0.006803	3100	28	3042	19	2955	28
BX4-7-18	0.124351	0.003005	6.159150	0.138189	0.359618	0.004067	2020	43	1999	20	1980	19
BX4-7-19	0.158379	0.002610	10.246692	0.176057	0.466902	0.004795	2439	28	2457	16	2470	21
BX4-7-20	0.167262	0.003205	4.249859	0.107805	0.185039	0.005126	2531	32	1684	21	1094	28
Sample BX6-2, altered tuffaceous siltstone												
BX6-2-01	0.066746	0.002206	1.164941	0.036014	0.126990	0.001630	831	69	784	17	771	13
BX6-2-02	0.067779	0.002552	1.188660	0.042467	0.127417	0.001697	861	78	795	20	773	10
BX6-2-03	0.064186	0.003060	1.118023	0.051167	0.127406	0.001996	748	106	762	25	773	11
BX6-2-04	0.063272	0.002768	1.100879	0.047454	0.126882	0.002268	717	94	754	23	770	13
BX6-2-05	0.065155	0.002714	1.149471	0.046761	0.127500	0.001748	789	82	777	22	774	10
BX6-2-06	0.160696	0.003240	10.095834	0.202013	0.453234	0.005505	2465	20	2444	19	2410	24
BX6-2-07	0.060556	0.001711	1.068600	0.031244	0.127108	0.001474	633	61	738	15	771	14
BX6-2-08	0.064315	0.001879	1.136180	0.031349	0.127394	0.001400	754	56	771	15	773	15
BX6-2-09	0.061124	0.001831	1.078050	0.032196	0.126843	0.001440	643	58	743	16	770	12
BX6-2-10	0.068700	0.002690	1.198712	0.039941	0.127129	0.001448	900	81	800	18	771	10
BX6-2-11	0.060483	0.001614	1.011210	0.025936	0.120446	0.001151	620	57	709	13	733	12
BX6-2-12	0.059990	0.001654	1.057898	0.030384	0.126487	0.001408	611	59	733	15	768	13
BX6-2-13	0.149029	0.002923	7.997563	0.228130	0.385502	0.008139	2335	24	2231	26	2102	38
BX6-2-14	0.063599	0.001679	1.118422	0.028301	0.127217	0.001456	728	56	762	14	772	13
BX6-2-15	0.061321	0.001559	1.079312	0.026916	0.126859	0.001294	650	56	743	13	770	12
BX6-2-16	0.168562	0.003590	10.880184	0.221052	0.467702	0.005609	2544	41	2513	19	2473	25
BX6-2-17	0.149069	0.002297	8.221946	0.148600	0.397428	0.004590	2336	26	2256	16	2157	21
BX6-2-18	0.063127	0.001825	1.106145	0.032917	0.126529	0.001556	722	61	756	16	768	10
BX6-2-19	0.155103	0.003208	8.872504	0.196418	0.411692	0.004403	2403	35	2325	20	2223	20
BX6-2-20	0.064722	0.002137	1.135386	0.038662	0.126498	0.001596	765	70	770	18	768	11
BX6-2-21	0.070838	0.002553	1.498025	0.056499	0.152866	0.002291	954	78	930	23	917	13
BX6-2-22	0.074745	0.003258	1.307145	0.055129	0.126310	0.001664	1061	87	849	24	767	10
BX6-2-23	0.061896	0.002108	1.088859	0.036091	0.126972	0.001466	672	74	748	18	771	15
BX6-2-24	0.068376	0.002104	1.072372	0.031395	0.114009	0.001745	880	63	740	15	696	10
BX6-2-25	0.082354	0.003120	1.474980	0.064047	0.126520	0.001646	1254	69	920	26	768	16
BX6-2-26	0.062737	0.002446	1.091429	0.041167	0.126044	0.001633	698	88	749	20	765	16
BX6-2-27	0.065036	0.002157	1.135803	0.035795	0.126979	0.001520	776	69	771	17	771	10
BX6-2-28	0.068622	0.001879	1.203461	0.033536	0.126290	0.001113	887	56	802	15	767	13
BX6-2-29	0.065394	0.002042	1.147297	0.034380	0.126998	0.001255	787	66	776	16	771	14
BX6-2-30	0.065427	0.001973	1.149656	0.034145	0.127188	0.001403	787	63	777	16	772	13

Note: $^{206}Pb/^{238}U$ ages for zircons younger than 1000 Ma and $^{206}Pb/^{207}Pb$ ages for those older than 1000 Ma were used for age interpretation in the text.

(6 pristine, 7 ablated) from sample BX4-7 yielded a mean (U–Th)/He age of 126.0 ± 4.9 Ma (MSWD = 1.0) (Fig. 8a), and twenty zircon grains (6 pristine, 14 ablated) from sample BX6-2 yielded a mean (U–Th)/He age of 122.2 ± 5.4 Ma (MSWD = 1.4) (Fig. 8b). The two mean ages are consistent within error, and all the thirty-three zircons combined yielded a mean age of 123.8 ± 3.8 Ma (MSWD = 1.2) (Fig. 8c). In addition, there was no correlation between U–Pb ages and (U–Th)/He ages in the two samples (Fig. 8d) – both Neoproterozoic (~770 Ma) and Paleoproterozoic (~1900–2500 Ma) zircon crystals revealed Early Cretaceous (U–Th)/He ages.

5. Discussion

5.1. Timing of Sb mineralization in South China

The metallogenic epoch of the giant Sb (Au–Hg) ore belt in South China is still under heated debate. Previous studies indicate three major age ranges for Sb mineralization within and around the Jiangnan Orogen: 435–380 Ma, 230–200 Ma and 160–130 Ma (Hu et al., 2016). The Sb–Au–W deposits in the Jiangnan Orogen could have formed during the Late Caledonian and the Late Triassic, evidenced by the Woxi Sb–Au–W deposit (scheelite Sm–Nd and quartz Ar–Ar ages, 420–402 Ma, Peng et al., 2003b) and Zhazixi W–Sb deposit (scheelite Sm–Nd age, 227.3 ± 6.2 Ma, Wang et al., 2012c). In contrast, the Sb-only and Sb–F deposits around the Jiangnan Orogen may have formed during Late Jurassic–Early Cretaceous, as evidenced by the Xikuangshan Sb deposit (syn-sulfide calcite Sm–Nd ages, 155.5 ± 1.1 and 124.1 ± 3.7 Ma, Peng et al., 2003a; zircon (U–Th)/He, 156–117 and 97–86 Ma, Fu et al., 2019a), Qinglong Sb deposit (calcite and fluorite Sm–Nd isochron ages, 148–142 Ma, Wang et al., 2012b) and Banxi Sb deposit (stibnite and arsenopyrite Sm–Nd and Rb–Sr isochron ages, ~130 Ma, Li et al., 2018c; zircon (U–Th)/He dating, 130–120 Ma, Fu et al., 2019b).

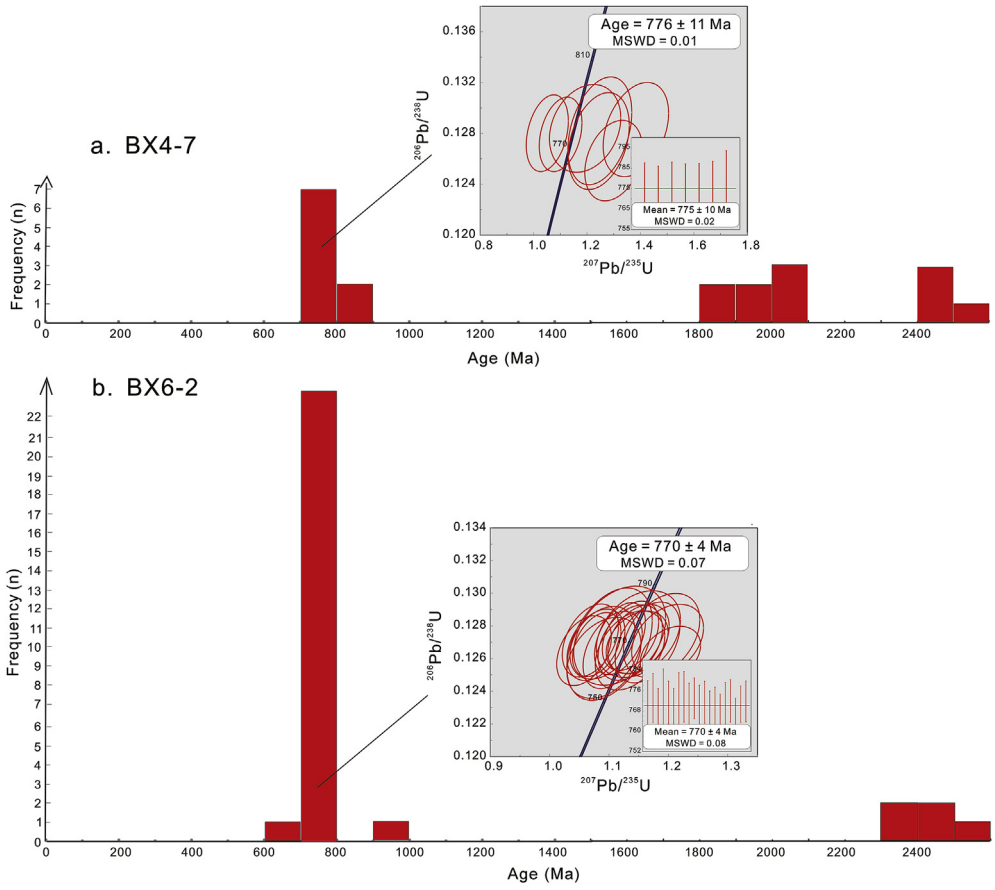

Fig. 6. Zircon U–Pb age variations of samples (a) BX4-7 and (b) BX6-2 from the Banxi Sb deposit.

Table 2
Zircon LA-MC-ICPMS Hf isotopic compositions of the Banxi Sb deposit.

Spot No.	$^{176}Yb/^{177}Hf$	2σ	$^{176}Lu/^{177}Hf$	2σ	$^{176}Hf/^{177}Hf$	2σ	Age (Ma)	$(^{176}Hf/^{177}Hf)_i$	$\varepsilon_{Hf}(t)$	T_{DM} (Ga)	T_{DM}^{C} (Ga)
Sample BX4-7, quartz-stibnite ore											
BX4-7-01	0.053941	0.000678	0.001736	0.000026	0.282053	0.000085	774	0.282028	-9.2	1.72	2.26
BX4-7-02	0.009742	0.000146	0.000301	0.000002	0.281247	0.000062	1955	0.281236	-10.7	2.74	3.24
BX4-7-03	0.023582	0.000351	0.000737	0.000004	0.281342	0.000075	2457	0.281307	3.3	2.65	2.76
BX4-7-04	0.024255	0.000475	0.000807	0.000004	0.281938	0.000078	776	0.281926	-12.8	1.84	2.48
BX4-7-05	0.016291	0.000592	0.000527	0.000024	0.282398	0.000066	773	0.282390	3.6	1.19	1.45
BX4-7-06	0.015193	0.000981	0.000438	0.000018	0.281284	0.000071	2054	0.281267	-7.4	2.70	3.11
BX4-7-07	0.011628	0.000177	0.000358	0.000004	0.281256	0.000069	2037	0.281242	-8.6	2.74	3.17
BX4-7-08	0.055682	0.000536	0.001899	0.000034	0.282495	0.000075	777	0.282467	6.4	1.10	1.28
BX4-7-09	0.020466	0.000203	0.000734	0.000020	0.281850	0.000071	775	0.281839	-15.9	1.95	2.67
BX4-7-10	0.026595	0.000973	0.000879	0.000038	0.282012	0.000071	778	0.281999	-10.2	1.74	2.32
Sample BX6-2, altered tuffaceous siltstone											
BX6-2-01	0.038162	0.000556	0.001377	0.000014	0.282216	0.000035	771	0.282196	-3.4	1.48	1.89
BX6-2-02	0.023488	0.000694	0.000857	0.000026	0.281836	0.000040	773	0.281824	-16.5	1.98	2.71
BX6-2-03	0.014420	0.000262	0.000505	0.000004	0.282111	0.000032	773	0.282104	-6.6	1.59	2.09
BX6-2-04	0.039272	0.001180	0.001395	0.000029	0.282278	0.000047	770	0.282258	-1.2	1.39	1.75
BX6-2-05	0.046547	0.001960	0.001604	0.000055	0.282628	0.000039	774	0.282605	11.2	0.90	0.97
BX6-2-06	0.017720	0.000284	0.000657	0.000015	0.281401	0.000027	2465	0.281370	5.7	2.56	2.62
BX6-2-07	0.099458	0.001866	0.003370	0.000042	0.282405	0.000039	771	0.282356	2.3	1.28	1.53
BX6-2-08	0.042764	0.000580	0.001445	0.000027	0.282134	0.000031	773	0.282113	-6.2	1.59	2.07
BX6-2-09	0.040586	0.000616	0.001414	0.000012	0.282235	0.000032	770	0.282215	-2.7	1.45	1.84
BX6-2-10	0.031930	0.000883	0.001105	0.000018	0.282131	0.000034	771	0.282115	-6.2	1.58	2.07
BX6-2-11	0.045818	0.000119	0.001588	0.000011	0.282183	0.000033	733	0.282161	-5.4	1.53	1.99
BX6-2-12	0.054250	0.001113	0.001763	0.000027	0.282595	0.000029	768	0.282570	9.8	0.95	1.05
BX6-2-13	0.025773	0.000240	0.000976	0.000012	0.281399	0.000039	2335	0.281356	2.2	2.59	2.74
BX6-2-14	0.055626	0.000654	0.001899	0.000019	0.282094	0.000032	772	0.282066	-7.9	1.67	2.17
BX6-2-15	0.021798	0.000482	0.000759	0.000011	0.282136	0.000035	770	0.282125	-5.9	1.56	2.04
BX6-2-16	0.023837	0.000552	0.000877	0.000012	0.281455	0.000038	2544	0.281412	9.1	2.50	2.48

Note: The spot No. is consistent with that in Table 1. $^{206}Pb/^{238}U$ ages for zircons younger than 1000 Ma and $^{206}Pb/^{207}Pb$ ages for those older than 1000 Ma were used in this table.

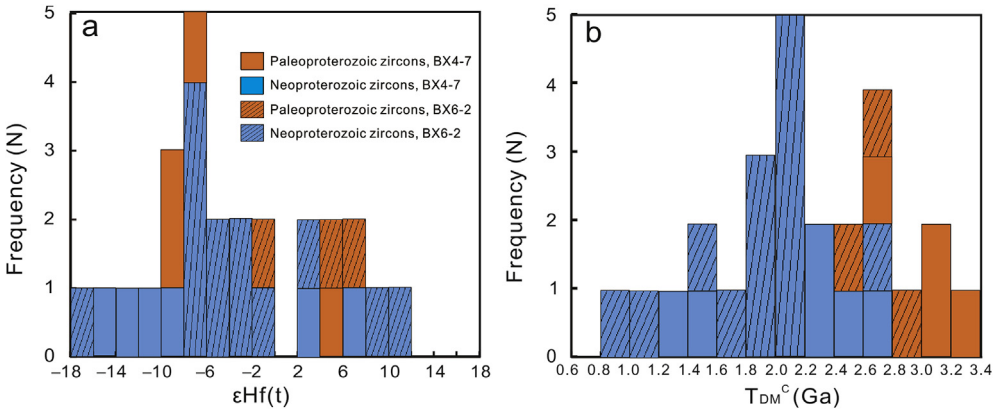

Fig. 7. Histograms of (a) zircon $\varepsilon_{Hf}(t)$ values and (b) T_{DM}^{C} ages from the Sb deposit.

Direct dating of Sb–Au low-temperature mineralization using (U–Th)/He geochronology has only been previously reported in one study (Fu et al., 2016). Previous research suggested that the Sb–Au deposits were epithermal-type with a shallow mineralization depth (Zhong et al., 2017), thus the temperature (~200 °C) required for resetting (U–Th)/He system in zircons should be related to hydrothermal activity. Since no tectonic events that could disturb the (U–Th)/He isotopic system were recorded in the Banxi region post-Late Jurassic–Early Cretaceous times (Wang et al., 2012b), the mean (U–Th)/He age of the zircons (123.8 ± 3.8 Ma) is interpreted to represent the timing of the latest stage of the Banxi Sb mineralization.

This age is not only close to the reported stibnite and arsenopyrite Sm–Nd and Rb–Sr isochron ages (~130 Ma) in Banxi (Li et al., 2018c) but also identical within uncertainty to that of the later Sb mineralization stage in the Xikuangshan deposit (124.1 ± 3.7 Ma, Peng et al., 2003a) and consistent with the age of the major Sb mineralization stage in the Banpo deposit (calcite Sm–Nd isochron age of 130.5 ± 3.0 Ma; Xiao, 2014). Though no contemporary magmatic rocks have been found in these regions, it cannot exclude the existence of deep rock mass which could have provided the heat for fluid circulation (Li et al., 2018c). The (U–Th)/He age also suggests that the Early Cretaceous (130–120 Ma) could be the most important mineralization epoch for the Sb deposits in South China and that the (U–Th)/He age of zircons separated from typical ore and altered country rock can reveal the timing of low-temperature mineralization.

5.2. Origin of the Sb deposits in South China

The genesis of the intense Sb (Au–Hg) mineralization in South China has been ascribed to many factors and processes, such as granitic magmatism (Peng and Frei, 2004; Liang et al., 2014), pre-concentration during sedimentary and diagenetic stages (Fan et al., 2004), deep circulation of meteoric water (Yang et al., 2006a), basement rock contribution (Yang et al., 2006b; Peng et al., 2008), sedimentary exhalative processes (Gu et al., 2007, 2012), and orogenic, deep non-magmatic crustal fluids (Zhu and Peng, 2015; Li et al., 2018c).

In this study, the age variation of zircons separated from quartz-stibnite ore (BX4-7) are consistent with those of the Banxi Group country rock (BX6-2). Moreover, the two age groups correspond to those of Banxi Group clastic rocks in the region, which typically falling into two age spans; 720–820 Ma and 1800–2500 Ma (Zhang et al., 2008a, b; Wang et al., 2010). This indicates that the all zircons in the quartz-stibnite ore sample were originally from the Banxi Group. In addition, the variable Hf isotopic compositions of the Banxi deposit (Neoproterozoic zircon $\varepsilon_{Hf}(t)$ = –16.5 to 11.2) is consistent with those of the Banxi Group in the region (Fig. 9a, b; Wang et al., 2010, 2012d; Meng et al., 2013), further proving that the zircons in the Banxi hydrothermal system came from the Banxi Group country rocks. These lines of evidence indicate that the Banxi Group country rocks played an important role in providing ore-forming materials (e.g., Sb and S) by fluid circulation, resulting in large-scale Sb mineralization in the Banxi area. The fluid circulation may have been trigged by the deep intrusion of magmatic rocks in the region; and previous isotopic data-set (S, Pb, Sr, Nd, He and Ar) of the Banxi deposit have documented that the ore-forming fluids were a mixture of dominantly deep basement-derived, solute-rich parent water mixed with a small amount of dilute, heated meteoric water (Li et al., 2018c). Detrital zircons were transported by channelized metal-bearing mineralizing fluids, but their U–Pb ages were not reset during low-temperature hydrothermal processes. Though contemporary granitic rocks (130–120 Ma) have not been found to be exposed in the typical Sb deposits from central-western Hunan, the recent geophysical exploration and drilling activity carried out by the Banxi mine have confirmed the existing of the deep magmatic bodies in the mineralization region. Moreover, recent studies have also indicated that the Late Jurassic–Early Cretaceous extensional event may provide favourable conditions for bringing deep intrusion of magmatic rocks in the central part of the South China Block (Li et al., 2014b; Hu and Peng, 2018; Wei et al., 2018).

The variable $\varepsilon_{Hf}(t)$ values and Hf model ages of the Neoproterozoic and Paleoproterozoic zircons in the quartz-stibnite ore and altered tuffaceous siltstone suggest a complex source provenance for the Banxi Group. The Hf isotopic model ages of detrital zircons with positive $\varepsilon_{Hf}(t)$ values may reveal multiple periods of juvenile crustal growth (Wang et al., 2017; Li et al., 2019c), during which initial ore-forming materials may have been initially enriched. These complex orogenic processes may have provided material basis for the large-scale low-temperature mineralization during Early Cretaceous, making the Banxi Group as one of the most important ore-bearing stratum in South China.

Including the Banxi Group, Precambrian basement rocks are not only the major component of the Jiangnan Orogen but also widely distributed beneath the covers of the Yangtze and Cathaysian Blocks around the Jiangnan Orogen (Zhang et al., 2016; Zhong et al., 2017). Recent research also suggests that the Sb–Hg abundance values (Hg = 0.36 ppm; Sb = 1.45 ppm) in Proterozoic basement rocks of South China are significantly higher than the average of the Earth's crust and granitic rocks (Liu et al., 2011); S, Pb, Sr and Nd isotopic analysis of representative Sb ores mostly point to the direct genetic connection to old basement rocks (Peng et al., 2003c; Yang et al., 2006b; Shen et al., 2011; Li et al., 2018c), and different types of Sb deposit in South China have distinct features reflecting differences in the nature and composition of the basement rocks (Hu et al., 2017). Combined with the results obtained in this study, it is reasonable to infer that Precambrian basement rocks were the major metal contributors for Sb mineralization in South China. In addition, the most current study (Li et al., 2019d) has documented that there are compositional differences between the Banxi Group fluid-altered (decolorized) and unaltered wall-rocks: the SiO_2, SO_3, LREE, Hf, Nb, Zr, Ta, Th, U, Mo, Sn and W have been increased in the altered

Table 3
Zircon (U–Th)/He isotopic compositions of the Banxi Sb deposit.

Zircon No.	^{232}Th (ng)	± (%)	^{232}Th (ppm)	^{238}U (ng)	± (%)	^{238}U (ppm)	^{147}Sm (ng)	± (%)	^{147}Sm (ppm)	He (ncc)	± (%)
Sample BX4-7, quartz-stibnite ore											
BX4-7-1	0.335	2.0	83.9	0.163	2.4	40.8	0.003	20.6	0.8	2.577	0.9
BX4-7-2	0.338	1.5	93.0	0.319	1.9	87.8	0.002	38.1	0.5	4.692	0.9
BX4-7-3	0.436	1.5	90.6	0.502	1.9	104.4	0.002	10.3	0.4	7.283	0.8
BX4-7-4	0.203	2.0	111.9	0.123	2.4	68.1	0.002	27.0	0.9	2.140	1.0
BX4-7-5	0.170	1.5	86.4	0.133	1.9	67.4	0.002	35.8	1.1	2.162	0.8
BX4-7-6	0.283	1.5	118.6	0.209	1.9	87.6	0.001	24.1	0.6	3.040	0.9
BX4-7-7	0.430	1.5	100.0	0.279	1.9	64.9	0.004	30.4	1.0	4.432	0.9
BX4-7-8	0.515	1.5	452.5	0.535	2.0	469.4	0.001	17.3	0.5	7.387	2.3
BX4-7-9	0.269	1.5	191.6	0.651	1.9	463.2	0.002	21.3	1.7	8.810	2.3
BX4-7-10	0.451	2.0	313.1	0.309	2.4	214.9	0.003	21.2	2.1	4.704	2.3
BX4-7-11	0.261	1.5	186.7	0.835	1.9	598.0	0.002	21.0	1.5	9.481	2.3
BX4-7-12	1.877	1.4	545.2	1.333	1.9	387.4	0.008	11.0	2.3	23.910	2.3
BX4-7-13	0.660	1.4	493.9	0.460	1.9	344.5	0.003	23.6	2.2	6.643	2.3
Sample BX6-2, altered tuffaceous siltstone											
BX6-2-1	0.168	1.5	56.6	0.154	1.9	52.1	0.003	20.1	1.2	2.029	1.9
BX6-2-2	0.126	1.5	58.5	0.100	1.9	46.6	0.002	47.7	0.8	1.430	2.0
BX6-2-3	0.134	1.5	63.0	0.091	1.9	42.9	0.002	39.1	1.0	1.344	1.9
BX6-2-4	0.051	2.0	26.8	0.046	2.4	24.3	0.004	29.0	2.2	0.645	2.0
BX6-2-5	0.136	1.5	65.3	0.135	1.9	64.9	0.003	39.0	1.3	2.194	2.0
BX6-2-6	0.170	1.5	42.3	0.238	1.9	59.2	0.003	16.8	0.7	2.976	1.9
BX6-2-7	0.311	1.5	115.6	0.326	1.9	120.9	0.002	25.2	0.9	4.281	1.9
BX6-2-8	0.173	2.0	91.6	0.140	2.4	74.3	0.001	5.6	0.5	2.024	1.9
BX6-2-9	0.235	1.5	114.8	0.200	1.9	97.7	0.009	14.6	4.3	2.443	2.0
BX6-2-10	0.102	1.5	69.0	0.098	1.9	66.3	0.002	27.9	1.1	1.222	2.0
BX6-2-11	0.143	1.5	56.8	0.128	1.9	50.9	0.002	35.4	0.8	2.006	2.0
BX6-2-12	0.070	2.0	43.8	0.074	2.4	46.1	0.002	32.0	1.5	1.000	2.1
BX6-2-13	0.081	1.6	94.3	0.076	1.9	89.5	0.002	30.2	2.0	1.068	1.9
BX6-2-14	0.181	1.5	176.7	0.143	1.9	139.6	0.004	23.6	4.0	2.037	0.9
BX6-2-15	0.242	2.0	385.7	0.197	2.4	313.4	0.001	12.4	1.9	2.591	2.3
BX6-2-16	0.389	1.5	394.5	0.398	1.9	404.2	0.001	27.8	1.3	5.681	2.3
BX6-2-17	0.270	1.5	291.8	0.243	1.9	262.6	0.002	20.6	2.0	2.976	2.2
BX6-2-18	0.225	1.5	327.3	0.210	1.9	305.8	0.001	27.8	2.1	2.776	2.3
BX6-2-19	0.192	2.0	163.4	0.696	2.4	591.7	0.002	24.0	1.8	8.864	2.3
BX6-2-20	0.379	1.5	539.1	0.546	1.9	776.2	0.003	14.7	4.8	5.418	2.3

Zircon No.	TAU (%)	Th/U	eU (ppm)	Raw He age (Ma)	±1σ (Ma)	Ft	± (%)	ES radius (μm)	Cor. He age (Ma)	±1σ (Ma)	U–Pb age (Ma)
Sample BX4-7, quartz-stibnite ore											
BX4-7-1	2.0	2.04	61	86.9	1.7	0.80	10	44	108.4	11.0	774
BX4-7-2	1.8	1.05	110	95.9	1.7	0.79	10	42	121.4	12.3	1955
BX4-7-3	1.8	0.86	126	98.2	1.8	0.79	10	41	124.6	12.7	2457
BX4-7-4	2.1	1.63	95	102.1	2.1	0.73	10	32	139.9	14.3	776
BX4-7-5	1.7	1.27	88	101.9	1.7	0.76	10	37	133.7	13.6	773
BX4-7-6	1.7	1.34	116	90.2	1.6	0.77	10	39	116.5	11.8	2054
BX4-7-7	1.7	1.53	89	95.0	1.6	0.78	10	40	121.4	12.3	2037
BX4-7-8	2.8	0.96	579	91.9	2.6	0.74	5	50	124.3	7.1	
BX4-7-9	2.9	0.41	512	100.5	2.9	0.73	5	48	137.9	7.9	
BX4-7-10	2.9	1.45	290	92.4	2.7	0.70	5	43	132.2	7.7	
BX4-7-11	2.9	0.31	646	86.4	2.5	0.71	5	44	122.2	7.0	
BX4-7-12	2.7	1.40	518	109.8	3.0	0.80	5	64	138.0	7.8	
BX4-7-13	2.7	1.42	463	88.1	2.4	0.75	5	53	116.8	6.6	
Sample BX6-2, altered tuffaceous siltstone											
BX6-2-1	2.5	1.08	66	85.5	2.1	0.79	10	42	108.1	11.1	771
BX6-2-2	2.5	1.25	61	90.2	2.2	0.73	10	32	123.2	12.7	723
BX6-2-3	2.4	1.46	58	89.3	2.2	0.68	10	27	132.2	13.6	773
BX6-2-4	2.8	1.09	31	91.1	2.5	0.73	10	32	124.8	12.9	770
BX6-2-5	2.5	1.00	81	106.8	2.7	0.79	10	41	136.0	14.0	774
BX6-2-6	2.5	0.71	70	87.2	2.2	0.74	10	34	117.5	12.1	2465
BX6-2-7	2.4	0.95	149	87.6	2.1	0.77	10	38	114.0	11.7	771
BX6-2-8	2.7	1.23	96	91.3	2.4	0.76	10	36	120.7	12.5	773
BX6-2-9	2.5	1.17	125	78.3	1.9	0.77	10	38	101.5	10.5	770
BX6-2-10	2.5	1.03	83	82.0	2.1	0.78	10	39	105.4	10.9	771
BX6-2-11	2.5	1.11	65	100.9	2.5	0.78	10	40	129.1	13.3	733
BX6-2-12	2.9	0.94	57	90.1	2.6	0.71	10	30	126.9	13.2	768
BX6-2-13	2.5	1.05	112	91.3	2.3	0.72	10	31	126.6	13.0	2335
BX6-2-14	1.8	1.26	182	89.8	1.6	0.76	10	37	117.7	12.0	772
BX6-2-15	3.0	1.22	406	83.3	2.5	0.62	5	34	134.3	7.8	
BX6-2-16	2.8	0.97	500	94.7	2.6	0.70	5	43	135.2	7.7	
BX6-2-17	2.7	1.10	333	79.2	2.2	0.67	5	40	117.6	6.7	
BX6-2-18	2.7	1.06	385	86.3	2.4	0.66	5	38	131.6	7.5	
BX6-2-19	3.2	0.27	634	97.5	3.1	0.72	5	46	136.3	8.1	
BX6-2-20	2.8	0.69	909	69.7	1.9	0.64	5	36	108.3	6.2	

Note: The grain No. is consistent with the spot No. in Table 2. ^{206}Pb/^{238}U ages for zircons younger than 1000 Ma and ^{206}Pb/^{207}Pb ages for those older than 1000 Ma were used in this table. eU = effective uranium concentration; eU = U + 0.235Th.

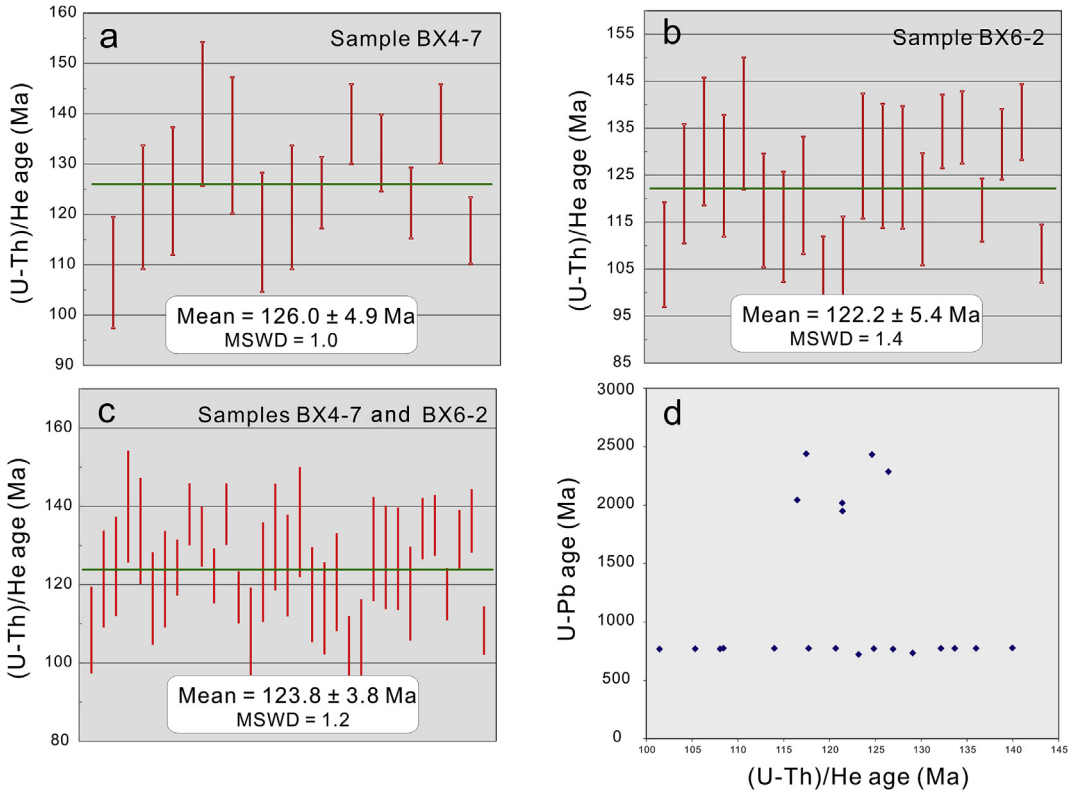

Fig. 8. Zircon (U–Th)/He dating results of (a) sample BX4-7, (b) sample BX6-2, (c) samples BX4-7 and BX6-2, and (d) (U–Th)/He ages vs. U–Pb ages from the Banxi Sb deposit.

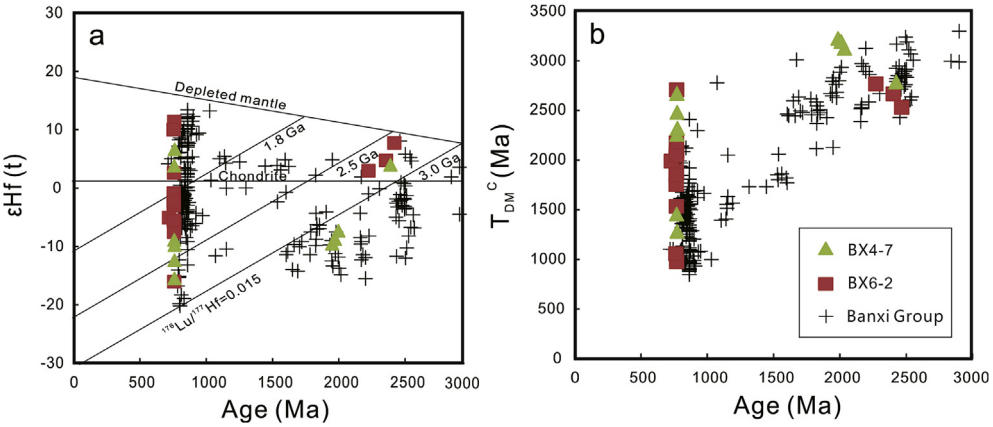

Fig. 9. Plots of age vs. $\varepsilon_{Hf}(t)$ (a) and T_{DM}^{C} (b) for the zircons from the Banxi Sb deposit. Zircon data of the Banxi Group clastic rocks (cross-shaped patterns) are from Wang et al. (2010), Wang et al. (2012d) and Meng et al. (2013).

wall-rocks, suggesting a deep basement metamorphic rocks-derived Si-rich alkaline brine for the fluid-rock interaction; the Fe_2O_3, MgO, MnO, TiO_2, Ba, Cs, Rb, As, Co, V, Ni, Sb, Sc, Cu, Pb and Zn have been leached out from the altered rocks, implying a material contribution of Banxi Group wall-rocks during the Sb mineralization process. The recent fluid inclusion microthermometry and H–O–S isotopic studies (Li et al., 2019d) also indicated that the thermodynamic conditions of fluid–rock interactions were low homogenization temperature (170–260 °C), low salinity (3–7 wt.% NaCl equiv.), low fluid density (0.72–0.93 g/cm^3) and low pH (5.59), and the mineralization occurred in a depth of 4.9 km. All of this further confirms the important role of Precambrian basement rocks during the large-scale Sb mineralization. Consequently, a final tectonic-metallogenic model is proposed to illustrate the mineralization process of the Banxi Sb deposit (Fig. 10).

5.3. Significance of integrated analysis of zircons

Variable types of zircons with multiple origin (e.g., magmatic, hydrothermal and metamorphic; detrital, inherited and captured) have been found in different types of ores from a wide range of deposits (e.g., Kerrich and King, 1993; Pelleter et al., 2007; Li et al., 2014a, 2017, 2018d; Sun et al., 2017; Jiang et al., 2018). Among them, detrital zircons are dominant in low-temperature mineralization (Qi et al., 2005; Li et al., 2006; Kanouo et al., 2018). Integrated analysis of detrital zircons has been used to reveal the genesis of ores. For example, integrated U–Pb and Lu–Hf analysis of detrital zircons (497–3409 Ma, peak population at 800–1000 Ma) in Pb–Zn ores from the Xianghualing deposit (South China) has revealed that circulation of evolved fluids through older sedimentary rocks led to Pb–Zn mineralization (Wu et al., 2018). In this

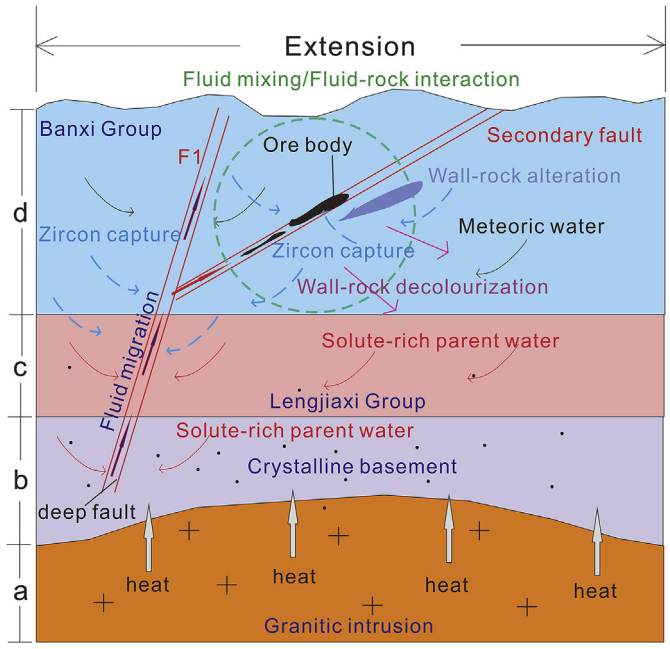

Fig. 10. A tectonic-metallogenic model illustrating the mineralization process of the Banxi Sb deposit. (a) Late Jurassic–Early Cretaceous extensional event provided favourable conditions for bringing a deep granitic intrusion; (b) basement rocks-derived solute-rich parent water was circulated by the granitic intrusion; (c) fluid migrated through the Lengjiaxi Group along the deep fault and captured some country rock zircons; (d) fluid mixing/fluid-rock interaction resulted in the Sb mineralization with the precipitation of country rock zircons, accompanied by wall-rock decolourization.

study, the first integrated U–Pb, Lu–Hf and (U–Th)/He analysis of single zircon grains from the Banxi Sb deposit has not only revealed the timing of low-temperature mineralization, but also revealed the genesis of the ores. Although the transport mechanisms for detrital zircons in low-temperature systems needs further study, integrated isotopic analysis shows a promise as a tool for the study of low-temperature mineralization.

6. Conclusions

A novel multi-analytical approach applying U–Pb, Lu–Hf and (U–Th)/He analyses to single zircons was successfully used here to unravel the genesis of low-temperature Sb (Au–Hg) deposits in Banxi, South China. Banxi Group country rocks (zircon U–Pb age = ~770 Ma, $\varepsilon_{Hf}(t) = -16.5$ to 11.2) played an important role in providing ore-forming materials by fluid circulation. Precambrian basement rocks were the major metal contributor for the Sb mineralization in South China.

Zircon (U–Th)/He ages define a tight cluster at 123.8 ± 3.8 Ma and record the age of the last low-temperature thermal event, interpreted to represent the timing of the latest mineralization stage of the Banxi Sb deposit. The Early Cretaceous (130–120 Ma) could therefore be the most important mineralization epoch for the Sb deposits in South China.

The integrated U–Pb and Lu–Hf analysis by LA-(MC)-ICPMS and conventional (U–Th)/He dating approach applied to single zircon crystals presented constrains the full thermal and genetic evolution of zircon from magmatic source, through crystallization and low-temperature cooling. This approach can be useful for dating low-temperature mineralization, but also for zircon provenance and other studies where a detailed understanding of zircon history may be beneficial.

Declaration of competing interest

The authors declare that they have no known competing financial interests or personal relationships that could have appeared to influence the work reported in this paper.

Acknowledgments

This work was co-financed by the National Natural Science Foundation of China (Grant No. 41502067) and the Fundamental Research Funds for the Central Universities, China University of Geosciences (Wuhan) (Grant No. CUG150612). We thank the John de Laeter Centre at Curtin University for access to the Low Temperature Thermochronology Facility. M.D. was supported by Australian Research Council Discovery funding scheme (DP160102427) and a Curtin Research Fellowship. We thank Dr. Vinod O. Samuel (Associate Editor) and anonymous reviewers for their useful comments that greatly improved the manuscript.

References

Andersen, T., 2002. Correction of common lead in U–Pb analyses that do not report ^{204}Pb. Chem. Geol. 192, 59–79.
Betsi, T.B., Lentz, D., McInnes, B., Evans, N.J., 2012. Emplacement ages and exhumation rates for intrusion-hosted Cu-Mo-Sb-Au mineral systems at Freegold Mountain (Yukon, Canada): assessment from U-Pb, Ar-Ar, and (U-Th)/He geochronometers. Can. J. Earth Sci. 49, 653–670.
Bouvier, A., Vervoort, J.D., Patchett, P.J., 2008. The Lu–Hf and Sm–Nd isotopic composition of CHUR: constraints from unequilibrated chondrites and implications for the bulk composition of terrestrial planets. Earth Planet. Sci. Lett. 273, 48–57.
Chen, X., Su, W.C., Huang, Y., 2016. He and Ar isotope geochemistry of ore-forming fluids for the Qinglong Sb deposit in Guizhou Province, China. Acta Petrol. Sin. 32, 3312–3320.
Chu, N.C., Taylor, R.N., Chavagnac, V., Nesbitt, R.W., Boella, R.M., Milton, J.A., German, C.R., Bayon, G., Burton, K., 2002. Hf isotope ratio analysis using multi-collector inductively coupled plasma mass spectrometry: an evaluation of isobaric interference corrections. J. Anal. Atomic Spectrom. 17, 1567–1574.
Cui, X., Zhu, W.B., Fitzsimons, I.C.W., Wang, X., Lu, Y.Z., Wu, X.H., 2017. A possible transition from island arc to continental arc magmatism in the eastern Jiangnan Orogen, South China: insights from a Neoproterozoic (870-860 Ma) gabbroic-dioritic complex near the Fuchuan ophiolite. Gondwana Res. 46, 1–16.
Cunningham, C.G., Zartman, R.E., McKee, E.H., Rye, R.O., Naeser, C.W., Sanjines, O., Ericksen, G.E., Tavera, F., 1996. The age and thermal history of Cerro Rico de Potosi, Bolivia. Miner. Depos. 31, 374–385.
Danišík, M., Stěpančíková, P., Evans, N.J., 2012. Constraining long-term denudation and faulting history in intraplate regions by multisystem thermochronology: an example of the Sudetic Marginal Fault (Bohemian Massif, central Europe). Tectonics 31, 1–19.
De Biévre, P., Taylor, P.D.P., 1993. Table of the isotopic compositions of the elements. Int. J. Mass Spectrom. Ion Process. 123, 149–166.
Evans, N.J., Byrne, J.P., Keegan, J.T., Dotter, L.E., 2005. Determination of uranium and thorium in zircon, apatite, and fluorite: application to laser (U-Th)/He thermochronology. J. Anal. Chem. 60, 1159–1165.
Fan, D.L., Zhang, T., Ye, J., 2004. The Xikuangshan Sb deposit hosted by the Upper Devonian black shale series, Hunan, China. Ore Geol. Rev. 24, 121–133.
Farley, K.A., Wolf, R.A., Silver, L.T., 1996. The effects of long alpha-stopping distances on (U-Th)/He ages. Geochem. Cosmochim. Acta 60, 4223–4229.
Farley, K.A., 2002. (U-Th)/He dating: techniques, calibrations, and applications. Rev. Mineral. Geochem. 47, 819–844.
Fu, S.L., Hu, R.Z., Chen, Y.W., Luo, J.C., 2016. Chronology of the Longshan Au-Sb deposit in central Hunan Province: constraints from pyrite Re-Os and zircon U-Th/He isotopic dating. Acta Petrol. Sin. 32, 3507–3517 (in Chinese with English abstract).
Fu, S., Hu, R., Batt, G.E., Danišík, M., Evans, N.J., Mi, X., 2019a. Zircon (U-Th)/He thermochronometric constraints on the mineralization of the giant Xikuangshan Sb deposit in central Hunan, South China. Miner. Depos. https://doi.org/10.1007/s00126-019-00906-3.
Fu, S., Hu, R., Yan, J., Lan, Q., Gao, W., 2019b. The mineralization age of the Banxi Sb deposit in Xiangzhong metallogenic province in southern China. Ore Geol. Rev. 112 https://doi.org/10.1016/j.oregeorev.2019.103033.
Griffin, W.L., Wang, X., Jackson, S.E., et al., 2002. Zircon chemistry and magma mixing, SE China: in-situ analysis of Hf isotopes, Tonglu and Pingtan igneous complexes. Lithos 61, 237–269.
Gu, X.X., Schulz, O., Vavtar, F., Liu, J.M., Zheng, M.H., Fu, S.H., 2007. Rare earth element geochemistry of the Woxi W–Sb–Au deposit, Hunan province, South China. Ore Geol. Rev. 31, 319–336.
Gu, X.X., Zhang, Y.M., Schulz, O., Vavtar, F., Liu, J.M., Zheng, M.H., Zheng, L., 2012. The Woxi W–Sb–Au deposit in Hunan, South China: an example of Late Proterozoic sedimentary exhalative (SEDEX) mineralization. J. Asian Earth Sci. 57, 54–75.
Harris, A.C., Dunlap, W.J., Reiners, P.W., Allen, C.M., Cooke, D.R., White, N.C., Campbell, I.H., Golding, S.D., 2008. Multimillion year thermal history of a porphyry copper deposit: application of U-Pb, ^{40}Ar/^{39}Ar and (U-Th)/He chronometers, Bajo de la Alumbrera copper-gold deposit, Argentina. Miner. Depos. 43, 295–314.
Hu, A., Peng, J., 2018. Fluid inclusions and ore precipitation mechanism in the giant Xikuangshan mesothermal antimony deposit, South China: conventional and infrared microthermometric constraints. Ore Geol. Rev. 95, 49–64.

Hu, R.Z., Peng, J.T., Ma, D.S., Su, W.C., Shi, C.H., Bi, X.W., Tu, G.Z., 2007. Epoch of large-scale low-temperature mineralizations in southwestern Yangtze massif. Miner. Deposits 26, 583–596 (in Chinese with English abstract).
Hu, R.Z., Fu, S.L., Xiao, J.F., 2016. Major scientific problems on low-temperature metallogenesis of South China. Acta Petrol. Sin. 32, 3239–3251 (in Chinese with English abstract).
Hu, R.Z., Fu, S.L., Huang, Y., Zhou, M.F., Fu, S.H., Zhao, C.H., Wang, Y.J., Bi, X.W., Xiao, J.F., 2017. The giant South China Mesozoic low-temperature metallogenic domain: reviews and a new geodynamic model. J. Asian Earth Sci. 137, 9–34.
Hu, Z.C., Liu, Y.S., Gao, S., Liu, W.G., Zhang, W., Tong, X.R., Lin, L., Zong, K.Q., Li, M., Chen, H.H., Zhou, L., Yang, L., 2012. Improved in situ Hf isotope ratio analysis of zircon using newly designed X skimmer cone and jet sample cone in combination with the addition of nitrogen by laser ablation multiple collector ICP-MS. J. Anal. Atomic Spectrom. 27, 1391–1399.
Jackson, S.E., Pearson, N.J., Griffin, W.L., Belousova, E.A., 2004. The application of laser ablation-inductively coupled plasma-mass spectrometry to in situ U–Pb zircon geochronology. Chem. Geol. 211, 47–69.
Jiang, W.C., Li, H., Wu, J.H., Zhou, Z.K., Kong, H., Cao, J.Y., 2018. A newly found biotite syenogranite in the Huangshaping polymetallic deposit, South China: insights into Cu mineralization. J. Earth Sci. 29 (3), 537–555.
Kanouo, N.S., Ngueutchoua, G., Kouske, A.P., Yongue, R.F., Venkatesh, A.S., 2018. Trace element and U-Pb core age for zircons from western Meiganga gold placer, Cameroon: their genesis and Archean-Proterozoic sources. Minerals 8. https://doi.org/10.3390/min8050194.
Kerrich, R., King, R., 1993. Hydrothermal zircon and baddeleyite in Val-d'Or Archean mesothermal gold deposits: characteristics, compositions, and fluid-inclusion properties, with implications for timing of primary gold mineralization. Can. J. Earth Sci. 30, 2334–2351.
Lee, J.K.W., Williams, I.S., Ellis, D.J., 1997. Pb, U and Th diffusion in natural zircon. Nature 390, 159–162.
Li, H., Watanabe, K., Yonezu, K., 2014a. Zircon morphology, geochronology and trace element geochemistry of the granites from the Huangshaping polymetallic deposit, South China: implications for the magmatic evolution and mineralization processes. Ore Geol. Rev. 60, 14–35.
Li, H., Sun, H.S., Wu, J.H., Evans, N.J., Xi, X.S., Peng, N.L., Cao, J.Y., Gabo-Ratio, J.A.S., 2017. Re–Os and U–Pb geochronology of the Shazigou Mo polymetallic ore field, Inner Mongolia: implications for Permian–Triassic mineralization at the northern margin of the North China Craton. Ore Geol. Rev. 83, 287–299.
Li, H., Li, J.W., Algeo, T.J., Wu, J.H., Cisse, M., 2018a. Zircon indicators of fluid sources and ore genesis in a multi-stage hydrothermal system: the Dongping Au deposit in North China. Lithos 314–315, 463–478.
Li, H., Wu, J.H., Evans, N.J., Jiang, W.C., Zhou, Z.K., 2018b. Zircon geochronology and geochemistry of the Xianghualing A-type granitic rocks: insights into multi-stage Sn-polymetallic mineralization in South China. Lithos 312–313, 1–20.
Li, H., Wu, Q.H., Evans, N.J., Zhou, Z.K., Kong, H., Xi, X.S., Lin, Z.W., 2018c. Geochemistry and geochronology of the Banxi Sb deposit: implications for fluid origin and the evolution of Sb mineralization in central-western Hunan, South China. Gondwana Res. 55, 112–134.
Li, H., Myint, A.Z., Yonezu, K., Watanabe, K., Algeo, T.J., Wu, J.H., 2018d. Geochemistry and U–Pb geochronology of the Wagone and Hermyingyi A-type granites, southern Myanmar: implications for tectonic setting, magma evolution and Sn–W mineralization. Ore Geol. Rev. 95, 575–592.
Li, H., Zhou, Z.K., Algeo, T.J., Wu, J.H., Jiang, W.C., 2019a. Geochronology and geochemistry of tuffaceous rocks from the Banxi group: implications for Neoproterozoic tectonic evolution of the southeastern Yangtze block, South China. J. Asian Earth Sci. 177, 152–176.
Li, H., Zhou, Z.K., Evans, N.J., Kong, H., Wu, Q.H., Xi, X.S., 2019b. Fluid–zircon interaction during low-temperature hydrothermal processes: implications for the genesis of the Banxi antimony deposit, South China. Ore Geol. Rev. https://doi.org/10.1016/j.oregeorev.2019.103137.
Li, H., Cao, J., Algeo, T.J., Jiang, W., Liu, B., Wu, Q., 2019c. Zircons reveal multi-stage genesis of the Xiangdong (Dengfuxian) tungsten deposit, South China. Ore Geol. Rev. https://doi.org/10.1016/j.oregeorev.2019.102979.
Li, H., Kong, H., Zhou, Z.K., Tindell, T., Tang, Y.Q., Wu, Q.H., Xi, X.S., 2019d. Genesis of the Banxi Sb deposit, South China: constraints from wall-rock geochemistry, fluid inclusion microthermometry, Rb–Sr geochronology, and H–O–S isotopes. Ore Geol. Rev. https://doi.org/10.1016/j.oregeorev.2019.103162.
Li, J.H., Zhang, Y.Q., Dong, S.W., Johnston, S.T., 2014b. Cretaceous tectonic evolution of South China: a preliminary synthesis. Earth Sci. Rev. 134, 98–136.
Li, J.X., Qin, K.Z., Li, G.M., Cao, M.J., Xiao, B., Chen, L., Zhao, J.X., Evans, N.J., McInnes, B.I.A., 2012. Petrogenesis and thermal history of the Yulong porphyry copper deposit, Eastern Tibet: insights from U-Pb and U-Th/He dating, and zircon Hf isotope and trace element analysis. Mineral. Petrol. 105, 201–221.
Li, W.L., Chen, Y.G., Zhao, Y.S., Zhang, G.L., Zhang, Y.J., Lu, Y.M., 2006. U-Pb isotopic determination by SHRIMP method for zirconium in gold-bearing quartz veins of Zhaishang gold deposit in Gansu Province and its geological meaning. Gold 7, 4–7 (in Chinese with English abstract).
Liang, Y., Wang, G.G., Liu, S.Y., Sun, Y.Z., Huang, Y.G., Hoshino, K., 2014. A study on the mineralization of the Woxi Au–Sb–W deposit, western Hunan, China. Resour. Geol. 65, 27–38.
Liu, X., Fan, H.R., Evans, N.J., Batt, G.E., McInnes, B.I.A., Yang, K.F., Qin, K.Z., 2014. Cooling and exhumation of the mid-Jurassic porphyry copper systems in Dexing City, SE China: insights from geo- and thermochronology. Miner. Depos. 49, 809–819.
Liu, Y.M., Yang, D.S., Yang, X.Q., Pang, B.C., 2011. Mercury and antimony abundances of sedimentary rocks in South China. Geotect. Metallogenia 35, 410–420 (in Chinese with English abstract).
Liu, Y.S., Hu, Z.C., Zong, K.Q., Gao, C.G., Gao, S., Xu, J., Chen, H.H., 2010. Reappraisement and refinement of zircon U-Pb isotope and trace element analyses by LA-ICP-MS. Chin. Sci. Bull. 55, 1535–1546.
Ludwig, K.R., 2003. User's Manual for Isoplot 3.00: A Geochronological Toolkit for Microsoft Excel. Berkeley Geochronology Center, p. 70. Special Publication, No. 4.
Marillo-Sialer, E., Woodhead, J., Hergt, J., Greig, A., Guillong, M., Gleadow, A., Evans, N., Paton, C., 2014. The zircon 'matrix effect': evidence for an ablation rate control on the accuracy of U–Pb age determinations by LA-ICP-MS. J. Anal. Atomic Spectrom. 29, 981–989.
Ma, D.S., 1999. Regional pattern of element composition and fluid character in medium-low temperature metallogenic province of South China. Miner. Deposits 18, 347–358 (in Chinese with English abstract).
McInnes, B.I.A., Evans, N.J., Fu, F.Q., Garwin, S., 2005. Application of thermochronology to hydrothermal ore deposits. Rev. Mineral. Geochem. 58, 467–498.
Meng, Q.X., Zhang, J., Geng, J.Z., Zhang, C.L., Huang, W.C., 2013. Zircon U-Pb age and Hf isotope compositions of Lengjiaxi and Baxi groups in middle Hunan province: implications for the Neoproterozoic tectonic evolution in South China. Chin. Geol. 40, 191–216 (in Chinese with English abstract).
Morel, M.L.A., Nebel, O., Nebel-Jacobsen, Y.J., Miller, J.S., Vroon, P.Z., 2008. Hafnium isotope characterisation of the GJ-1 zircon reference material by solution and laser-ablation MC-ICPMS. Chem. Geol. 255, 231–235.
Pelleter, E., Cheilletz, A., Gasquet, D., Mouttaqi, A., Annich, M., El Hakourd, A., Deloule, E., Féraude, G., 2007. Hydrothermal zircons: a tool for ion microprobe U–Pb dating of gold mineralization (Tamlalt-Menhouhou gold deposit—Morocco). Chem. Geol. 245, 135–161.
Peng, B., Frei, R., 2004. Nd–Sr–Pb isotopic constraints on metal and fluid sources in W–Sb–Au mineralization at Woxi and Liaojiaping (Western Hunan, China). Miner. Depos. 39, 313–327.
Peng, J.T., Hu, R.Z., Burnard, P.G., 2003a. Samarium–neodymium isotope systematics of hydrothermal calcites from the Xikuangshan antimony deposit (Hunan, China): the potential of calcite as a geochronometer. Chem. Geol. 200, 129–136.
Peng, J.T., Hu, R.Z., Zhao, J.H., Fu, Y.Z., Lin, Y.X., 2003b. Scheelite Sm-Nd dating and quartz Ar-Ar dating for Woxi Au-Sb-W deposit, western Hunan. Chin. Sci. Bull. 48, 2640–2646.
Peng, J.T., Hu, R.Z., Jiang, G.H., 2003c. Samarium-Neodymium isotope system of fluorites from the Qinglong antimony deposit, Guizhou Province: constraints on the mineralizing age and ore-forming materials' sources. Acta Petrol. Sin. 19, 785–791.
Peng, J.T., Zhang, D.L., Hu, R.Z., Wu, M.J., Lin, Y.X., 2008. Sm-Nd and Sr isotope geochemistry of hydrothermal scheelite from the Zhazixi W-Sb deposit, western Hunan. Acta Geol. Sin. 82, 1514–1521 (in Chinese with English abstract).
Qi, J.Z., Li, L., Yuan, S.S., Liu, Z.J., Liu, D.Y., Wang, Y.B., Li, Z.H., 2005. A SHRIMP U-Pb chronological study of zircons from quartz veins of Yangshan gold deposit, Gansu Province. Miner. Deposits 24, 141–150 (in Chinese with English abstract).
Reiners, P.W., 2005. Zircon (U-Th)/He thermochronometry. Rev. Mineral. Geochem. 58, 151–179.
Shen, N.P., Peng, J.T., Hu, R.Z., Liu, S., Coulson, I.M., 2011. Strontium and lead isotopic study of the carbonate-hosted Xujiashan antimony deposit from Hubei province, South China: implications for its origin. Resour. Geol. 61, 52–62.
Soderlund, U., Patchett, J.P., Vervoort, J.D., Isachsen, C.E., 2004. The ^{176}Lu decay constant determined by Lu–Hf and U–Pb isotope systematics of Precambrian mafic intrusions. Earth Planet. Sci. Lett. 219, 311–324.
Song, G., Wang, X., Shi, X., Jiang, G., 2017. New U-Pb age constraints on the upper Banxi Group and synchrony of the Sturtian glaciation in South China. Geosci. Front. 8 (5), 1161–1173.
Su, J.B., Dong, S.W., Zhang, Y.Q., Li, Y., Chen, X.H., Ma, L.C., Chen, J.S., 2017. Orogeny processes of the western Jiangnan Orogen, South China: insights from Neoproterozoic igneous rocks and a deep seismic profile. J. Geodyn. 103, 42–56.
Sun, H.S., Li, H., Evans, N.J., Yang, H., Wu, P., 2017. Volcanism, mineralization and metamorphism at the Xitieshan Pb–Zn deposit, NW China: insights from zircon geochronology and geochemistry. Ore Geol. Rev. 88, 289–303.
Vervoort, J.D., Blichert-Toft, J., 1999. Evolution of the depleted mantle: Hf isotope evidence from juvenile rocks through time. Geochem. Cosmochim. Acta 63, 533–556.
Wang, W., Wang, F., Chen, F., Zhu, X., Xiao, P., Siebel, W., 2010. Detrital zircon ages and Hf-Nd isotopic composition of neoproterozoic sedimentary rocks in the Yangtze block: constraints on the deposition age and provenance. J. Geol. 118, 79–94.
Wang, D.H., Qin, Y., Wang, C.H., Chen, Y.C., Gao, L., 2012a. Mineralization pedigree for epithermal Hg, Sb, Au deposits in Guizhou Province—taking the Dachang Sb deposit, the Zimudang Au deposit and the Luanyantang Hg deposit for examples. Geotect. Metallogenia 36, 330–336 (in Chinese with English abstract).
Wang, J.S., Wen, H., Fan, H.F., Zhu, J.J., 2012b. Sm-Nd geochronology, REE geochemistry and C and O isotope characteristics of calcites and stibnites from the Banian antimony deposit, Guizhou Province, China. Geochem. J. 46, 393–407.
Wang, P.M., Yu, J.H., Sun, T., Ling, H.F., Chen, P.R., Zhao, K.D., Chen, W.F., Liu, Q., 2012d. Geochemistry and detrital zircon geochronology of Neoproterozoic sedimentary rocks in eastern Hunan Province and their tectonic significance. Acta Petrol. Sin. 28, 3841–3857.
Wang, Y.L., Chen, Y.C., Wang, D.H., Xu, J., Chen, Z.H., 2012c. Scheelite Sm-Nd dating of the Zhazixi W-Sb deposit in Hunan and its geological significance. Chin. Geol. 39, 1339–1344 (in Chinese with English abstract).
Wang, Y.L., Xu, J., Zhang, C.Q., Wang, C.H., Chen, Z.H., Huang, F., 2014. Summary of metallogenic regularities of antimony deposits in China. Acta Geol. Sin. 88, 2208–2215 (in Chinese with English abstract).
Wang, J.Q., Shu, L.S., Santosh, M., 2017. U-Pb and Lu-Hf isotopes of detrital zircon grains from Neoproterozoic sedimentary rocks in the central Jiangnan Orogen, South China: implications for Precambrian crustal evolution. Precambrian Res. 294, 175–188.

Wei, W., Song, C., Hou, Q.L., Chen, Y., Faure, M., Yan, Q.R., Liu, Q., Sun, J.F., Zhu, H.F., 2018. The Late Jurassic extensional event in the central part of the South China Block - evidence from the Laoshan'ao shear zone and Xiangdong Tungsten deposit (Hunan, SE China). Int. Geol. Rev. 60, 1644–1664.

Wiedenbeck, M., Hanchar, J.M., Peck, W.H., Sylvester, P., Valley, J., Whitehouse, M., Kronz, A., Morishita, Y., Nasdala, L., Fiebig, J., Franchi, I., Girard, J.P., Greenwood, R.C., Hinton, R., Kita, N., Mason, P.R.D., Norman, M., Ogasawara, M., Piccoli, P.M., Rhede, D., Satoh, H., Schulz-Dobrick, B., Skar, O., Spicuzza, M.J., Terada, K., Tindle, A., Togashi, S., Vennemann, T., Xie, Q., Zheng, Y.F., 2004. Further characterisation of the 91500 zircon crystal. Geostand. Geoanal. Res. 28, 9–39.

Wu, J.H., Li, H., Algeo, T.J., Jiang, W.C., Zhou, Z.K., 2018. Genesis of the Xianghualing Sn–Pb–Zn deposit, South China: a multi-method zircon study. Ore Geol. Rev. 102, 220–239.

Xiao, X.G., 2014. Geochronology, Ore Geochemistry and Genesis of the Banpo Antimony Deposit, Guizhou Province, China. Ph.D thesis, Kunming University of Science and Technology, Kunming, pp. 1–138 (in Chinese with English abstract).

Xie, G., Mao, J., Bagas, L., Fu, B., Zhang, Z., 2018. Mineralogy and titanite geochronology of the Caojiaba W deposit, Xiangzhong metallogenic province, southern China: implications for a distal reduced skarn W formation. Miner. Depos. https://doi.org/10.1007/s00126-018-0816-2.

Xu, D., Deng, T., Chi, G., Wang, Z., Zou, F., Zhang, J., Zou, S., 2017. Gold mineralization in the Jiangnan Orogenic Belt of South China: geological, geochemical and geochronological characteristics, ore deposit-type and geodynamic setting. Ore Geol. Rev. 88, 565–618.

Yang, D.S., Shimizu, M., Shimazaki, H., Li, X.H., Xie, Q.L., 2006b. Sulfur isotope geochemistry of the supergiant Xikuangshan Sb deposit, central Hunan, China: constraints on sources of ore constituents. Resour. Geol. 56, 385–396.

Yang, R.Y., Ma, D.S., Bao, Z.Y., Pan, J.Y., Cao, S.L., Xia, F., 2006a. Geothermal and fluid flowing simulation of ore-forming antimony deposits in Xikuangshan. Sci. China Ser. D Earth Sci. 49, 862–871.

Zeng, Q.T., Evans, N.J., McInnes, B.I.A., Batt, G.E., McCuaig, C.T., Bagas, L., Tohver, E., 2013. Geological and thermochronological studies of the Dashui gold deposit, West Qinling Orogen, Central China. Miner. Depos. 48, 397–412.

Zhang, D.L., Huang, D.Z., Zhang, H.F., Wang, G.Q., Du, G.F., 2016. Chronological framework of basement beneath the Xiangzhong Basin: evidence by U-Pb ages of detrital zircons from Xikuangshan. Acta Petrol. Sin. 32, 3456–3468.

Zhang, Q.R., Li, X.H., Feng, L.J., Huang, J., Song, B., 2008a. A new age constraint on the onset of the Neoproterozoic glaciations in the Yangtze Platform, South China. J. Geol. 116, 423–429.

Zhang, S.H., Jiang, G.Q., Dong, J., Han, Y.G., Wu, H.C., 2008b. New SHRIMP U-Pb age from the Wuqiangxi formation of Banxi group: implications for rifting and stratigraphic erosion associated with the early Cryogenian (Sturtian) glaciation in South China. Sci. China Ser. D Earth Sci. 51, 1537–1544.

Zhao, G.C., 2015. Jiangnan Orogen in South China: developing from divergent double subduction. Gondwana Res. 27, 1173–1180.

Zhao, G.C., Cawood, P.A., 2012. Precambrian geology of China. Precambrian Res. 222–223, 13–54.

Zhong, J., Pirajno, F., Chen, Y.J., 2017. Epithermal deposits in South China: geology, geochemistry, geochronology and tectonic setting. Gondwana Res. 42, 193–219.

Zhu, Y.N., Peng, J.T., 2015. Infrared microthermometric and noble gas isotope study of fluid inclusions in ore minerals at the Woxi orogenic Au–Sb–W deposit, western Hunan, South China. Ore Geol. Rev. 65, 55–69.